



Synergistic effect of photocatalytic U(VI) reduction and chlorpyrifos degradation by bifunctional type-II heterojunction MOF525@BDMTp with high carrier migration performance

Xin Liu ^{a,b}, Zhi-Hai Peng ^b, Lan Lei ^b, Rui-Xiang Bi ^b, Cheng-Rong Zhang ^b, Qiu-Xia Luo ^b, Ru-Ping Liang ^{b,*}, Jian-Ding Qiu ^{a,b,**}

^a State Key Laboratory of Nuclear Resources and Environment, East China University of Technology, Nanchang 330013, PR China

^b School of Chemistry and Chemical Engineering, Nanchang University, Nanchang 330031, PR China



ARTICLE INFO

Keywords:

Covalent organic frameworks
Metal organic frameworks
Carrier mobility
Heterojunction
Photocatalyst

ABSTRACT

The radioactive ion U(VI) and organophosphorus pollutants in sewage do great harm to the ecological environment and human health. Bifunctional photocatalyst MOF525@BDMTp was prepared by in-situ covalent bridging method, and U(VI) and chlorpyrifos (CP) were removed by one-to-two strategy. MOF525@BDMTp had high carrier migration performance and conformed to the type-II heterojunction. Under light conditions, electrons were transferred from MOF525 to BDMTp due to the action of the built-in electric field, increasing the electron density of BDMTp and thus activating the U(VI) binding sites. BDMTp interacted with S and N atoms in CP to promote its hydrolysis and oxidation by h^+ and $\cdot\text{O}_2$. Thus, MOF525@BDMTp guaranteed the simultaneous reduction of U(VI) on BDMTp and the oxidation of CP on MOF525. Therefore, designing functional integrated composites is an effective means to improve the photocatalytic performance of composite materials in complex environments.

1. Introduction

Radioactive wastes contained in industrial production and mining wastewater released into the natural environment will have adverse effects on the ecological environment and human health development [1]. Excessive intake of uranium can lead to the accumulation of uranium in the liver and kidney, causing biological dysfunction [2]. Therefore, the removal of uranium from wastewater is of great significance to human health. The problem of radioactive contamination can be effectively solved by reducing highly toxic U(VI) to low-toxic and low-fluidity U(IV) through efficient and energy-saving photocatalytic method [3]. However, in addition to metal ions in complex water bodies, water polluted by the abuse and unreasonable disposal methods of organophosphorus (OPs) also cause serious damage to the ecosystem. Chlorpyrifos (CP), as a widely used OPs pesticide, can combine with acetylcholinesterase and destroy body metabolism, leading to cramps, diarrhea, paralysis and even death [4,5]. At present, there are some problems in the removal of CP, such as incomplete degradation and long

degradation time, so it is very important to explore efficient degradation methods of CP [6,7]. Therefore, the development of bifunctional materials for photocatalytic reduction of U(VI) and degradation of CP can effectively solve the problem of environmental pollution caused by multiple factors.

Metal organic frameworks (MOFs), which are prepared by central metal ions and organic ligands, have flexible functions, customizable structures, high porosity and design surfaces, and have broad application prospects in the field of photocatalysis [8,9]. Compared with traditional inorganic photocatalysts, MOFs ligands are adjustable as light absorbers, and metal exchange at the nodes can enhance the uniqueness of photoinduced electron transfer [10,11]. However, the single material has the disadvantage of easy photoelectron-hole recombination, and coupling of two semiconductors with matching band gap has been proved to be a feasible method to inhibit photoelectron-hole recombination. Therefore, the construction of heterojunction is an effective way to improve performance relative to the single semiconductor photocatalyst [12–14].

* Corresponding author.

** Corresponding author at: State Key Laboratory of Nuclear Resources and Environment, East China University of Technology, Nanchang 330013, PR China.

E-mail addresses: rpliang@ncu.edu.cn (R.-P. Liang), jdqiu@ncu.edu.cn (J.-D. Qiu).

In order to maximize the inherent properties of MOFs, it can be combined with covalent organic frameworks (COFs) that have similar properties and are synthesized from light elements and reversible covalent bonds [15,16]. COFs are advanced organic semiconductor components, which can be used as a selective adsorption carrier due to the adjustability of functional groups in the monomer [17]. Due to the particularity of topological structure, COFs can form ordered diffusion and transmission channels [18]. In addition, the wide light absorption and fast carrier migration performance of COFs also make the premise of photocatalysis [19,20]. The development of multi-functional MOFs-COFs composites is one of the effective ways to improve the properties of porous materials [21]. When MOFs and COFs are integrated together, the two can not only complement each other in performance, but also obtain unprecedented performance that can exceed the known MOFs or COFs-based composites. Although the research progress of MOFs/COFs composites has been made, it is still in its infancy.

Herein, a bifunctional composite structure MOF525@BDMTp with covalent bridge of MOFs and COFs was synthesized for photocatalytic reduction of U(VI) and degradation of CP. CP is adsorbed on BDMTp by weak interaction and decomposes into small molecules in photo-degradation. U(VI) is coordinated with a photoactivated functional group and then reduced by photogenerated electrons. The formation of type-II heterojunction at the interface prevents the electron-hole recombination and ensures the simultaneous reduction of U(VI) on BDMTp and the oxidation of CP on MOF525. In addition, the presence of U(VI) and CP improves the photocatalytic performance of MOF525@BDMTp for each of them.

2. Experimental section

2.1. Chemicals and characterization

The reagents were not further treated. Detailed information about reagents and instrument characterizations was shown in [Supporting Information \(SI\)](#).

2.2. Synthesis of MOF525

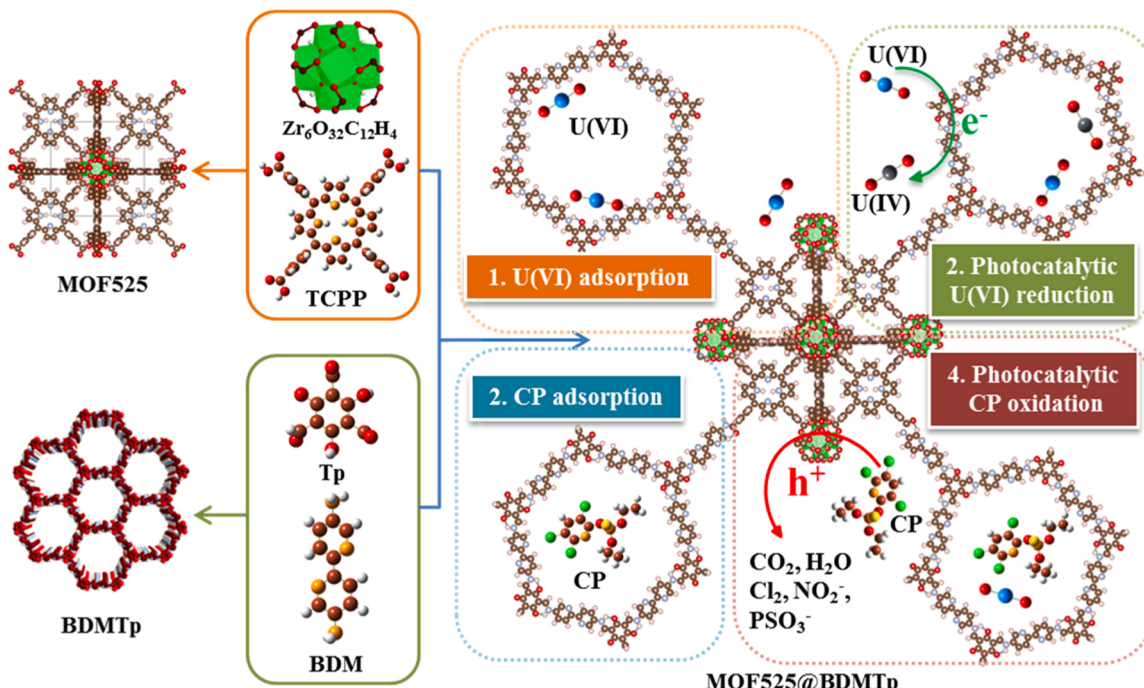
$\text{ZrOCl}_2 \bullet 8(\text{H}_2\text{O})$ (105.0 mg, 0.32 mmol) and benzoic acid (2.70 g, 0.02 mol) were dispersed in glass bottles containing *N,N*-dimethylformamide (DMF, 8 mL). The reactants were completely dissolved by ultrasound for 30 min and transferred to a reactor. Tetra(4-carboxyphenyl)porphyrin (TCPP, 47 mg, 0.06 mmol) was added to the above solution and reacted at 80 °C for 24 h. After the reaction, the precipitation was cooled to room temperature, washed three times with DMF and acetone, soaked in acetone for one day. Then it was filtered and vacuum dried at 60 °C for 12 h to obtain purple powder MOF525.

2.3. Synthesis of BDMTp

2,4,6-triformylphloroglucinol (Tp, 63.0 mg, 0.30 mmol) and 2,2'-bipyridine-5,5'-diamine (BDM, 83.7 mg, 0.45 mmol) were added to 20 mL Pyrex tube with a mixture of mesitylene (2 mL) and 1,4-dioxane (2 mL). Next, acetic acid aqueous solution (0.6 mL, 6 mol L⁻¹) was added to facilitate the catalytic reaction. After vacuum sealing and heating at 120 °C for 3 days, orange-red precipitate BDMTp was obtained.

2.4. Synthesis of MOF525@BDMTp

MOF525 (50.0 mg), BDM (83.7 mg, 0.45 mmol), 2-(7-azabenzotriazol-1-yl)-*N,N,N',N'*-tetramethyluronium hexafluorophosphate (HATU, 100 mg), and *N,N*-diisopropylethylamine (DIPEA, 60 μL) were dispersed in anhydrous DMF and subjected to ultrasonic reaction for 4 h. The above mixture was filtered and washed to obtain the precipitation. The precipitation and Tp (63.0 mg, 0.30 mmol) were dispersed in the mixture of mesitylene (2 mL), 1,4-dioxane (2 mL), and acetic acid aqueous solution (0.6 mL, 6 M), and then transferred to 20 mL Pyrex tubes. The purplish red precipitate MOF525@BDMTp was obtained under the same conditions as the synthetic BDMTp. The mass ratios of MOF525 and BDMTp in composite were 1:4, 1:2, and 1:1, respectively. The samples prepared by physical mixing of MOF525 and BDMTp were labeled as MOF525+ BDMTp.



Scheme 1. The synthesis diagram of MOF525@BDMTp and the mechanism diagram of removing U (VI) and CP.

2.5. Removal experiment of U(VI) and CP

U(VI) removal experiment: The catalyst (5 mg) was added to 20 mL aqueous solution containing a certain U(VI) concentration (50–300 mg L⁻¹). The samples were irradiated with ultraviolet/visible (UV/Vis) light for 4 h after reaching the equilibrium of adsorption and desorption. Finally, the filtrate after filtering through a 0.22 μm membrane filter was analyzed by ICP-MS to determine the U(VI) concentration. The formula R% = (C₀ - C_e)/C₀ × 100% was used to calculate the removal rate of U(VI), where C₀ and C_e were the initial and equilibrium concentrations of U(VI), respectively.

CP removal experiment: The catalyst (5 mg) was added to the solution (20 mL) containing CP with 50 mg L⁻¹. After reaching adsorption-desorption equilibrium, the system was exposed to UV/Vis light for 30 min, and 0.5 mL suspension was extracted at certain intervals and filtered by 0.22 μm membrane filter. The filtrate was collected and CP concentration was detected by ultraviolet spectrophotometer. CP removal rate formula is R% = (C₀ - C_e)/C₀ × 100%, where C₀ and C_e were the initial and equilibrium concentrations of CP, respectively. A pseudo-first-order kinetic model was used to fit the experimental data, and the formula was ln(q_e - q_t) = lnq_e - k₁t, where q_t and q_e (mg g⁻¹) represented the adsorption capacity at different time and equilibrium time (t, min), and k₁ (min⁻¹) represented the pseudo-first-order rate constant.

3. Results and discussion

3.1. Structure and morphology characterization

In this paper, the metal organic framework MOF525 was synthesized by ZrOCl₂·8(H₂O) and tetra(4-carboxyphenyl)porphyrin (TCPP). Cubic cells were constructed with zirconia unit Zr₆O₄(OH)₄ as metal nodes and TCPP as connecting units. MOF525 cell was composed of Zr₆O₄(OH)₄ units with 8 shared angles and TCPP units with 6 shared surfaces [22, 23]. The powder X-ray diffraction (PXRD) data simulated by Materials Studio were matched with the PXRD data of MOF525. The cell parameters a = 19.2 Å, b = 18.7 Å, c = 18.9 Å, pore size was 18.7 Å, Rp

= 0.5%, and Rwp = 1.5%. MOF525 had strong characteristic diffraction peaks at 4.7°, 6.6°, 8.1°, and 9.3° (2θ), corresponding to its (100), (110), (111), and (020) crystal planes, respectively. The results showed that MOF525 has good crystallinity (Fig. 1a). Secondly, the structure of BDMTp synthesized by 2,4,6-triformylresorcinol (Tp) and 2,2'-bipyridine-5,5'-diamine (BDM) was analyzed by PXRD. BDMTp had three characteristic diffraction peaks at 3.5°, 6.1°, and 27.1° (2θ), which were attributed to its (100), (110), and (001) crystal planes, respectively. By comparing the BDMTp model constructed by Materials Studio with the experimental data, Rp = 0.9% and Rwp = 1.3% were obtained after Pawley refining, indicating that the structure of COF was consistent with the AA stacking model and had good crystallinity (Fig. 1b). In addition, the bonding mode of the composite was characterized by Fourier transform infrared spectroscopy (FT-IR). The disappearance of -NH₂ and the displacement of C=O also indicate the condensation of Tp and BDM (Fig. S1) [24]. Next, the structure of the composite was characterized by PXRD. MOF525 @BDMTp showed the characteristic diffraction peaks of both, indicating the successful synthesis of the composite (Fig. 1c). Furthermore, the appearance of C-N (1231 cm⁻¹) and N-H (1570 cm⁻¹) in the amide group indicated that BDMTp covalently bonded with the carboxylic acid group in MOF525 (Fig. S2). The morphologies of the materials were characterized by scanning electron microscopy (SEM). As shown in Fig. 1d, MOF525 presented a regular cuboid shape with a smooth surface, while BDMTp was obviously different from MOF525 and cross-linked in a fibrous form (Fig. 1e). It is exciting that MOF525 @BDMTp presented a cluster-like structure, which is related to the covalently linked growth of COF on the surface of MOF525 as a core (Fig. 1f).

3.2. Photoelectric activity

Excellent photoelectric performance is the prerequisite for realizing high efficiency photocatalytic activity [25]. In order to investigate the photoelectric activity of the catalyst, UV/Vis diffuse reflection absorption spectrum was used to characterize the light absorption properties of the material [26]. The optical absorption edge of BDMTp was less than 600 nm, while the optical absorption edge of MOF525 was greater than

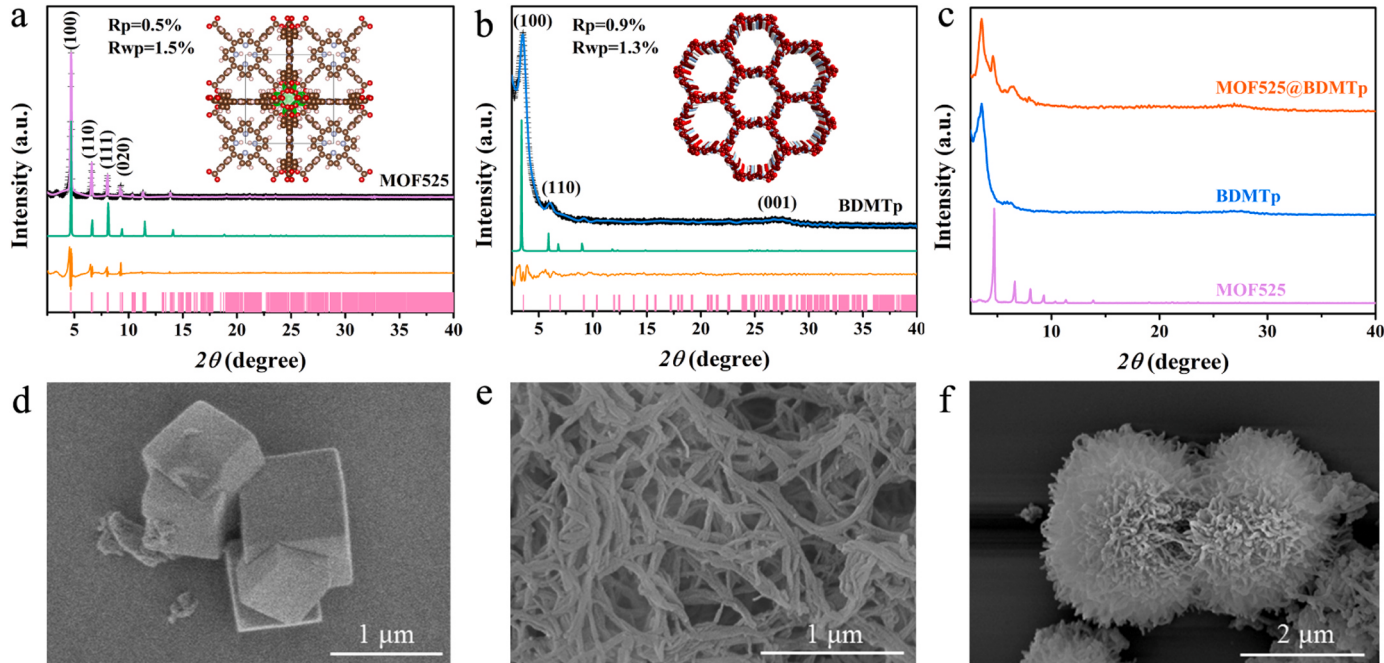


Fig. 1. The PXRD patterns for (a) MOF525 and (b) BDMTp, including experimental data (black crosses), Pawley refinement curve (purple and blue line), simulation data (green line), refinement difference (orange line), and Bragg position (pink bars). (c) The PXRD patterns for MOF525@BDMTp. SEM images of (d) MOF525, (e) BDMTp, and (f) MOF525@BDMTp.

700 nm. MOF525 had a wider optical absorption range than BDMTp. Due to the increased light absorption capacity in the presence of MOF525, the MOF525@BDMTp absorption edge was shifted to 700 nm (Fig. 2a). The band gaps (E_g) of BDMTp, MOF525, and BDMTp@MOF525 calculated by Kubelka-Munk function were 2.30, 1.80, and 1.82 eV, respectively (Fig. S3) [27,28]. Mott-Schottky method was used to test the flat-band potential of BDMTp and MOF525, and the slope of the curves was positive, indicating that both of them were N-type semiconductors (Fig. 2b) [29]. The conduction potential (E_{CB}) of BDMTp and MOF525 was -0.78 and -0.87 V (vs. NHE), respectively. Based on $E_{VB}-E_{CB}=E_g$, the valence band potential (E_{VB}) of BDMTp and MOF525 could be calculated to be 1.52 and 0.93 V (vs. NHE) (Fig. 2c) [25].

The charge transfer properties of each material were then studied. According to EIS curve analysis, MOF525@BDMTp had the smallest charge transfer resistance, indicating that the combination of the two promoted charge transfer, which may be related to the spontaneous electron flow caused by Fermi energy level difference between MOF525 and BDMTp (Fig. 2d) [30]. In addition, it can be seen from the photocurrent intensity that MOF525@BDMTp had the strongest photocurrent response, indicating that the composite material had a higher current density, because the heterogeneous structure formed by the two made charge separation easier (Fig. 2e). Especially, the photocurrent of MOF525@BDMTp attenuated slowly rather than disappeared instantly after stopping illumination, so it had the characteristics of "electronic sponge" for storing and transmitting electrons, which was also beneficial to the photocatalytic reaction [31,32]. The average lifetimes of MOF525, BDMTp and MOF525@BDMTp fitted according to fluorescence attenuation curves were 2.43, 0.71, and 0.41 ns, respectively (Fig. 2f). The shortened fluorescence lifetime of the composite indicated that energy and electron transfer occurred between MOF525 and BDMTp, and the faster the carrier transfer [30,33,34].

3.3. Removal of U(VI) and CP

To explore the synergistic effect of photocatalytic removal of U(VI) and CP, different proportions of MOF525 @BDMTp were first used for photocatalytic removal of U(VI). When MOF525: BDMTp = 1: 2, the removal rate of U(VI) was the highest, which was caused by the synergistic effect of the number of adsorption sites and electron transfer ability between MOF525 and BDMTp (Fig. S4) [35]. The 3D response surface model (RSM) was used to describe the influence of the interaction between variables on their response variables, and then the key variables and the optimal conditions were explored. In the process of photocatalytic removal of U(VI) and CP, three variables that greatly affect photocatalytic removal of U(VI) were selected in this study: Initial concentration of U(VI) (A), initial concentration of CP (B), and pH (C) of solution (Table S1). The peak intensity of U(VI) removal rate was used as an index to investigate the photocatalytic degradation efficiency. Based on Box-Behnken experiment design, three factors and three levels were selected to design the response surface experiment using $2k^{-1}$ factor in the Design-Expert statistical analysis software. Analysis of Variance (ANOVA) was used to evaluate the applicability and significance of the fitting model (Table S2). Adjusted $R^2=0.993$ and predicted $R^2=0.948$ were similar, indicating that the model was well fitted. According to the P values in the table, the P values of A, B, C, AB, AC, BC, A^2 , B^2 , and C^2 were all less than 0.0500, indicating that the above factors were significant [36,37]. According to the above studies, the decrease of pH was unfavorable to the removal of U(VI), but the increase of CP content could compensate for the adverse effect of the decrease of pH on the removal of U(VI), which was related to the increase of e^- utilization rate due to the consumption of h^+ by oxidizing CP (Fig. 3a-c). In addition, MOF525 @BDMTp had a separation coefficient (K_d) of 1.1×10^5 for U (VI) in the presence of five-fold competitive metal ions (Fig. S5), and anions in solution had a weak effect on U(VI) removal rate (Fig. S6). The results showed that MOF525 @BDMTp had excellent ion selectivity, which was related to its specific selection sites.

The isotherm removal study showed that MOF525@BDMTp had the

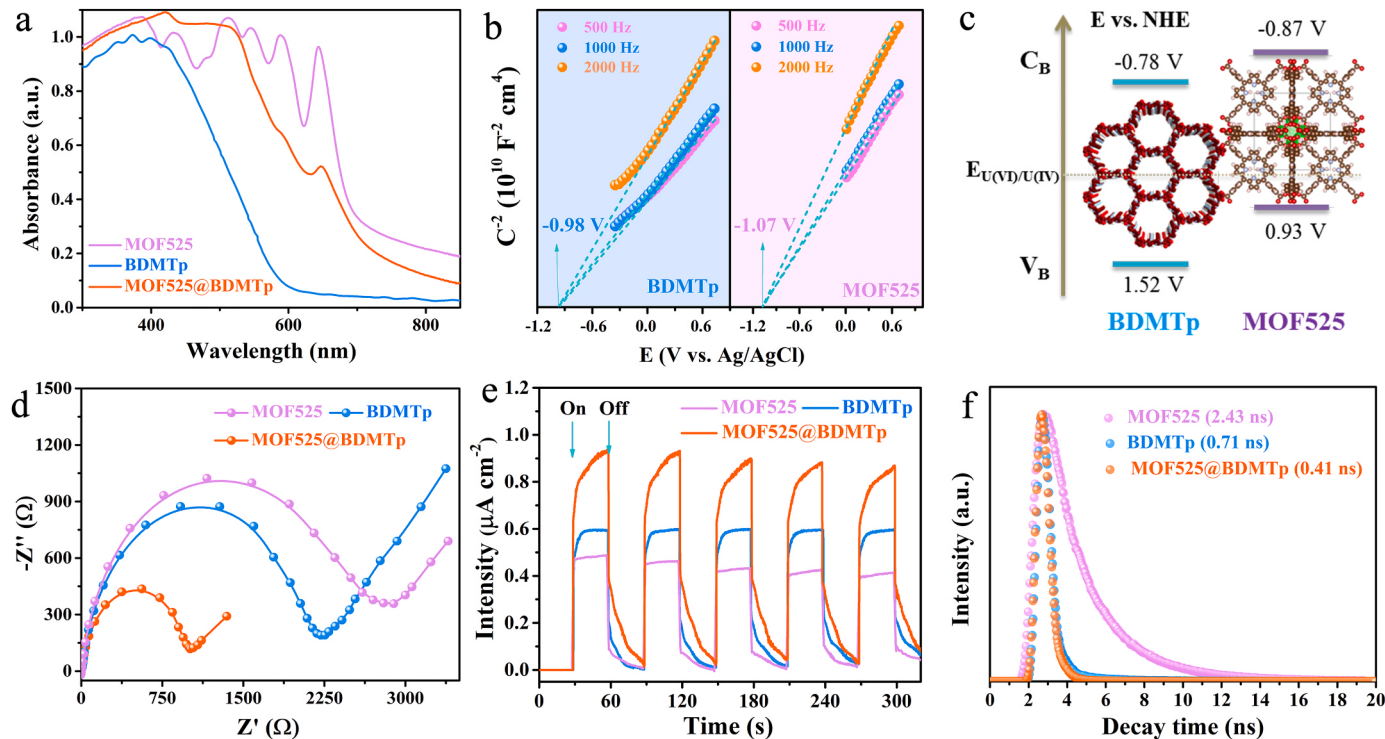


Fig. 2. (a) UV/Vis absorption spectra of MOF525, BDMTp, and MOF525@BDMTp, respectively. (b) Mott-Schottky plots of MOF525 and BDMTp. (c) Band structure of MOF525 and BDMTp. (d) EIS curves, (e) transient photocurrent response, and (f) PL decay curves of MOF525, BDMTp, and MOF525@BDMTp, respectively.

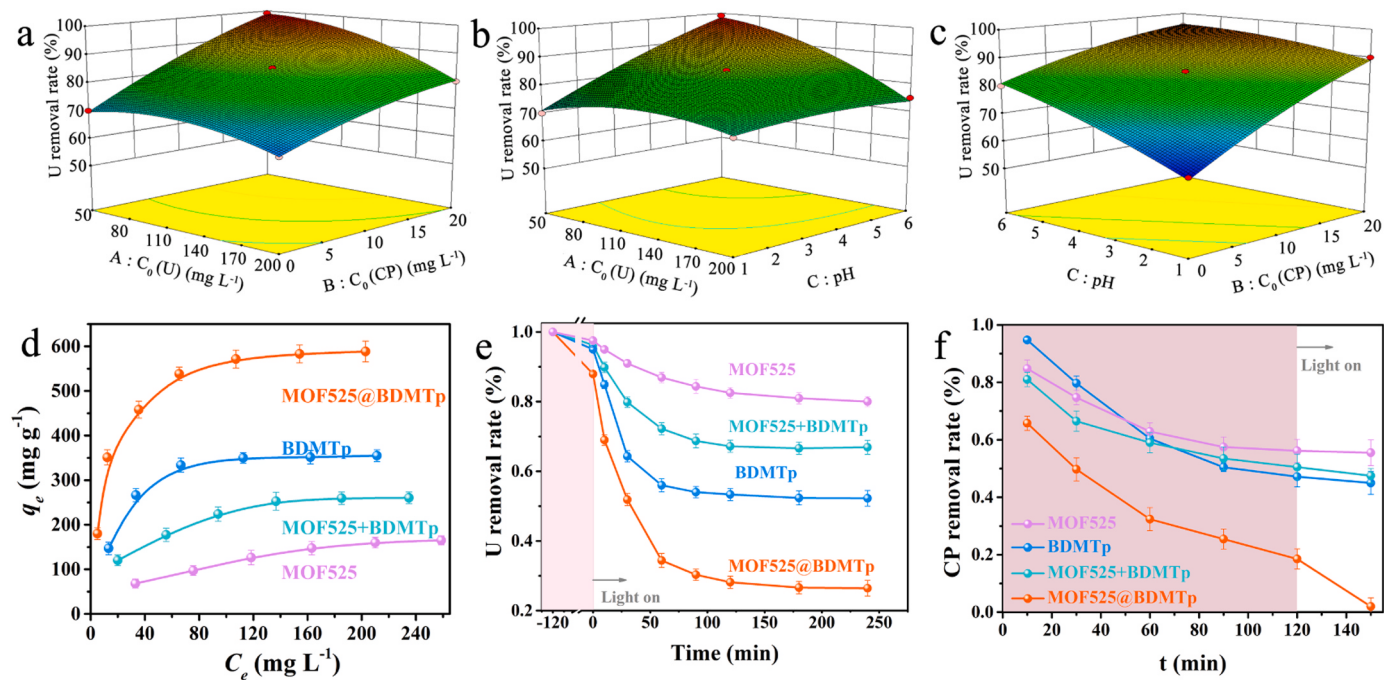


Fig. 3. 3D response surface optimization diagram for MOF525@BDMTp: (a) C_0 (U) vs. C_0 (CP); (b) C_0 (U) vs. pH; (c) C_0 (CP) vs. pH. (d) Removal isotherm diagram of U(VI) by MOF525, BDMTp, MOF525@BDMTp, and MOF525@BDMTp. The photocatalytic removal rate of (e) U(VI) and (f) CP by MOF525, BDMTp, MOF525@BDMTp, and MOF525@BDMTp.

highest slope, so MOF525@BDMTp had the strongest affinity with U (VI). Compared with MOF525 (222.2 mg g⁻¹), BDMTp (400.0 mg g⁻¹), and MOF525+BDMTp (333.3 mg g⁻¹), MOF525@BDMTp had a U(VI) removal capacity of 625.0 mg g⁻¹, indicating that electron-hole separation and transfer of the composite promoted photocatalytic reduction of U(VI) (Fig. 3d). Langmuir linear fitting showed that the fitting data of all materials presented good linearity, indicating the monolayer adsorption process ($R^2 \geq 0.99$) (Fig. S7 and Table S3). The introduction of MOF525 increased the range of light absorption, and the introduction of BDMTp increased the active sites. The heterogeneous structure formed by the combination of the two increased the electron-hole separation. These advantages led to the efficient U(VI) reduction performance of MOF525@BDMTp [38]. The low adsorption capacity of BDMTp in the dark may be due to the active sites (-N, -O) need to be activated under light, which was related to the change of electron density after excitation. According to the kinetic data, all four materials could reach equilibrium within 120 min, and all conformed to the pseudo-second-order kinetic model ($R^2 > 0.99$), which indicated that U (VI) had chemical coordination with the material surface groups (Fig. 3e, S8, and Table S4). Compared with Redox-COF1 [39] and ZnFe₂O₄ [40], MOF525@BDMTp had a higher U(VI) removal capacity. In addition, the equilibrium time for MOF525@BDMTp was shorter for those of Fe@ZIF-8 [41] and g-C₃N₄/TiO₂ [3] (Table S5).

Then, the adsorption and photodegradation of CP by various materials were explored. The removal rate of CP by MOF525@BDMTp reached 99.8%, which was related to the enhancement of CP adsorption and h⁺ oxidation by electron transfer of materials (Fig. 3f). MOF525@BDMTp had the best adsorption effect, because electrons flow from BDMTp to MOF525 due to the electron attraction performance of MOF525 under dark conditions. BDMTp had partial positive charge and CP had negative charge on the surface. Therefore, the electrostatic affinity of MOF525@BDMTp to CP increased. Kinetic data showed that CP adsorption conformed to the pseudo-first-order kinetic model ($R^2 \geq 0.99$), and the main effect of MOF525@BDMTp on CP was physical adsorption (Fig. S9). It can be seen that light was very important for CP degradation, and its removal rate could reach 99.8%. Therefore, MOF525@BDMTp had a higher CP removal capacity and removal rate

compared with those of CuFe₂O₄/MIL-101(Fe) [5] and nHAP@CF-GO/ZnR [42].

3.4. Mechanism of removal of U (VI) and CP

The interaction mode of U(VI) with the material was analyzed by X-ray photoelectron spectroscopy (XPS). The samples that reacted with U (VI) in dark and light were named MOF525@BDMTp-U_{ads} and MOF525@BDMTp-U_{pho}, respectively (Fig. 4a). The U 4 f peak appeared in both dark and light XPS spectra, and the intensity of U 4 f peak in MOF525@BDMTp-U_{pho} was greater than that in MOF525@BDMTp-U_{ads}, indicating that light promoted the U(VI) adsorption and reduction (Fig. S10 and S11). Compared with the N 1 s XPS spectra of MOF525@BDMTp-U_{ads} and MOF525@BDMTp, the binding energies of pyridinic-N, C=N, pyrrolic-N and C-N all shifted towards the direction of high binding energy, indicating the interaction between N-site and U (VI) (Fig. S12 and S13) [43]. The appearance of U-N peak in MOF525@BDMTp-U_{pho} indicated that illumination enhanced the activity of N-site and promoted the coordination of N-site and U(VI) (Fig. 4b). According to the XPS characterization of O 1 s, the binding energies of Zr-O, C=O, C-O and -OH in MOF525@BDMTp-U_{ads} and MOF525@BDMTp-U_{pho} all increased compared with that of MOF525@BDMTp, indicating the existence of coordination interaction between O-site and U(VI) (Fig. S14 and S15) [44,45]. The appearance of U-O bond indicated that the affinity between O and U (VI) increased under light and the catalytic reduction performance of the material was enhanced, which was related to the increase of electron density around O under light (Fig. 4c). Uranium mainly existed in the form of U(VI) during the adsorption process, and U(VI) and U(VI) coexisted after illumination, which was because the illumination enhanced the affinity between the active site and U(VI), and at the same time realized the process of U(VI) reduction to U(VI) on the catalyst (Fig. 4d and S16).

In the dark, the sample after MOF525@BDMTp reacted with CP was named MOF525@BDMTp-CP_{ads}. The appearance of P 2 p peak in XPS indicated that the material had adsorption effect on CP (Fig. 4e). By comparing N 1 s in MOF525@BDMTp-CP_{ads} and MOF525@BDMTp, it was found that the N 1 s binding energies of C=N and pyrrolic-N

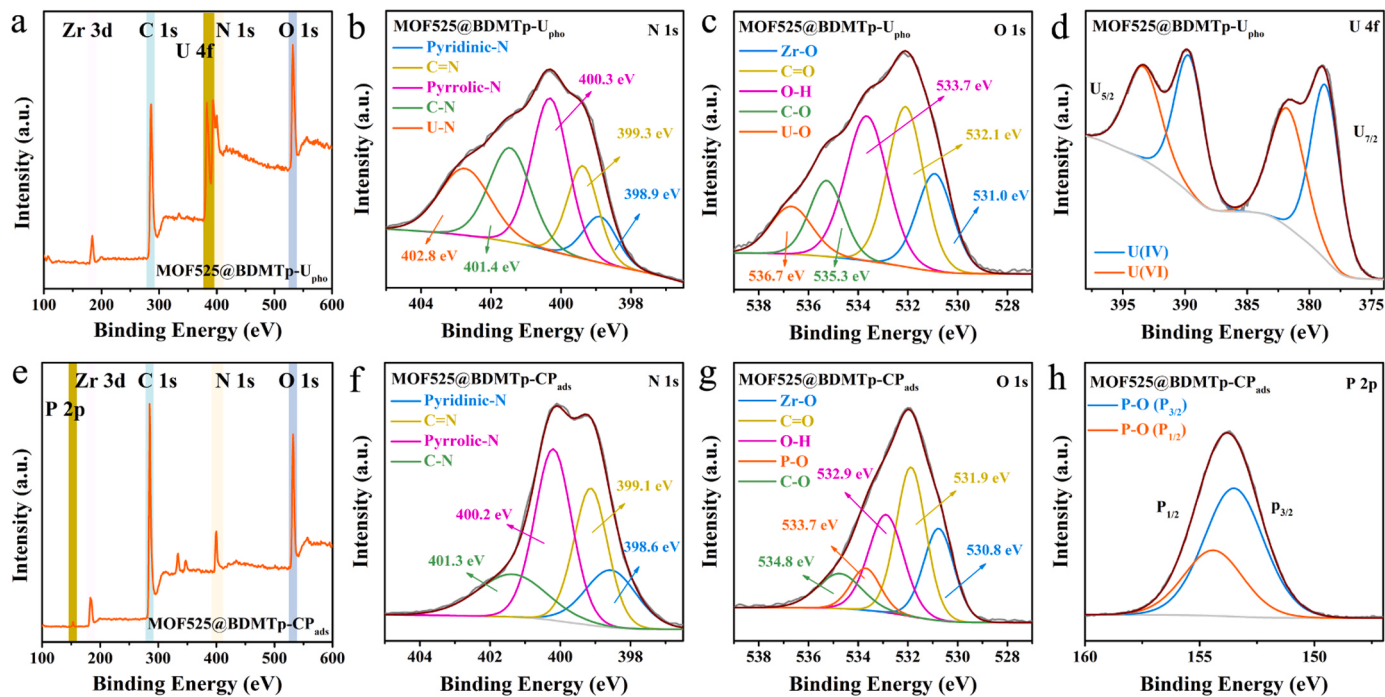


Fig. 4. (a) The XPS survey spectra of MOF525@BDMTp-U_{pho}. High-resolution XPS spectra of MOF525@BDMTp-U_{pho}: (b) N 1 s, (c) O 1 s, and (d) U 4 f. (e) The XPS survey spectra of MOF525@BDMTp-CP_{pho}. High-resolution XPS spectra of MOF525@BDMTp-CP_{pho}: (f) N 1 s, (g) O 1 s, and (h) P 2p.

remained unchanged, while the binding energies of C-N and pyridinic-N increased (Fig. 4f). The results showed that C-N and pyridinic-N had weak interaction on CP. The increase of C-O binding energy in O 1 s indicated that C-O had a weak interaction with CP (Fig. 4g) [42]. P-O peaks also appeared in O 1 s and P 2 p, indicating that MOF525@BDMTp can adsorb CP (Fig. 4h).

It can be seen from van der Waals surface electrostatic potential that the C-N position had positive electric property and the P-S of CP had negative electricity (Fig. 5a). Moreover, CP had a weak interaction with BDMTp according to the independent gradient model (IGM) (Fig. 5b). And the adsorption energy of BDMTp for U(VI) was $-682.63 \text{ kJ mol}^{-1}$ by DFT calculation (Fig. 5c). To explore the electron transfer direction and the type of heterojunction between MOF525 and BDMTp, the binding energy change of Zr 3d in MOF525@BDMTp under dark and light conditions was first measured by in-situ XPS, which was due to the presence of C, N, and O elements in MOF525 and BDMTp. The binding energy of Zr 3d increased by 0.3 eV under light action, which indicated that photogenerated electrons were transferred from MOF525 to BDMTp (Fig. S17). Next, the electrostatic potentials of MOF525 (001) and BDMTp (100) were calculated using DFT (Fig. 5d, e). The work function of MOF525 was larger than that of BDMTp, which had a higher Fermi energy level (E_F). Thus, when the two were connected through covalent bond, electrons will spontaneously diffuse from BDMTp to MOF525, resulting in the accumulation of electrons at the interface of MOF525 and the loss of electrons in the BDMTp layer. Furthermore, an internal electric field (E) directed towards MOF525 was formed at the interface and band bending occurred [24]. Both MOF525 and BDMTp in MOF525@BDMTp can be excited to produce electron-holes under UV/Vis irradiation. Due to band bending and internal electric field, electrons on C_B of MOF525 tended to transfer to C_B of BDMTp and accumulated at N- and O- sites. The holes on V_B of BDMTp tended to transfer to the V_B of MOF525. In summary, the band structure and electron transfer mode are combined with type-II heterojunction (Fig. 5f). At the same time, the existence of type-II heterojunction promoted the separation of photogenerated electron-hole. The complexed U (VI) at the active site was reduced to U(IV) at C_B of BDMTp. In addition, BDMTp binded to the S and N atoms of CP through weak interactions

such as van der Waals forces, inducing electron polarization, weakening the interaction between trichloropyridine and thiogroups, and destroying the P-O bond by electron migration. The oxygen atoms in the water molecule interacted with the P atoms, and CP hydrolyzed to produce 3, 5,6-trichloro-2-pyridinol (TCP) and diethyl thiophosphate (DETP). TCP and DETP were further mineralized by REDOX reactions of reactive species (h^+ and $\cdot O_2$) and thus degraded to CO_2 , H_2O , Cl_2 , NO_2 , and PSO_3^{2-} (Fig. S18) [46–48].

3.5. Practical application of MOF525@BDMTp

The practical application effect of MOF525@BDMTp was studied in wastewater containing U(VI) and CP. MOF525@BDMTp exhibited excellent photocatalytic selectivity and cycling performance, and more than 95.1% of U(VI) was absorbed and reduced by the photocatalyst under light (Fig. 6a). After five times of use, the U(VI) removal rate of regenerated MOF525@BDMTp remained above 90.0%, and the removal rate of CP was more than 94.0% (Fig. 6b). Therefore, the photocatalysis of MOF525@BDMTp has good application potential for simultaneous removal of U(VI) and CP from real water environment.

4. Conclusion

Bifunctional photocatalyst MOF525@BDMTp with MOF525 as core and BDMTp as shell have been synthesized in-situ by covalent bond bridging. Electrons flow spontaneously from BDMTp to MOF525 due to differences in Fermi energy levels under dark conditions, causing the BDMTp to be positively charged and creating an internal electric field at the interface. The negatively charged surface of CP interacts more easily with the BDMTp, thus improving the adsorption affinity. In addition, electrons are transferred from MOF525 to BDMTp due to the action of the built-in electric field under light conditions, increasing the electron density of BDMTp and thus activating the U(VI) binding site. Moreover, the formation of type-II heterojunction improves electron-hole separation and carrier migration speed, and ensures the simultaneous reduction of U(VI) on BDMTp and the oxidation of CP on MOF525. MOF525@BDMTp had a removal rate of 625.0 mg g^{-1} for U(VI) and

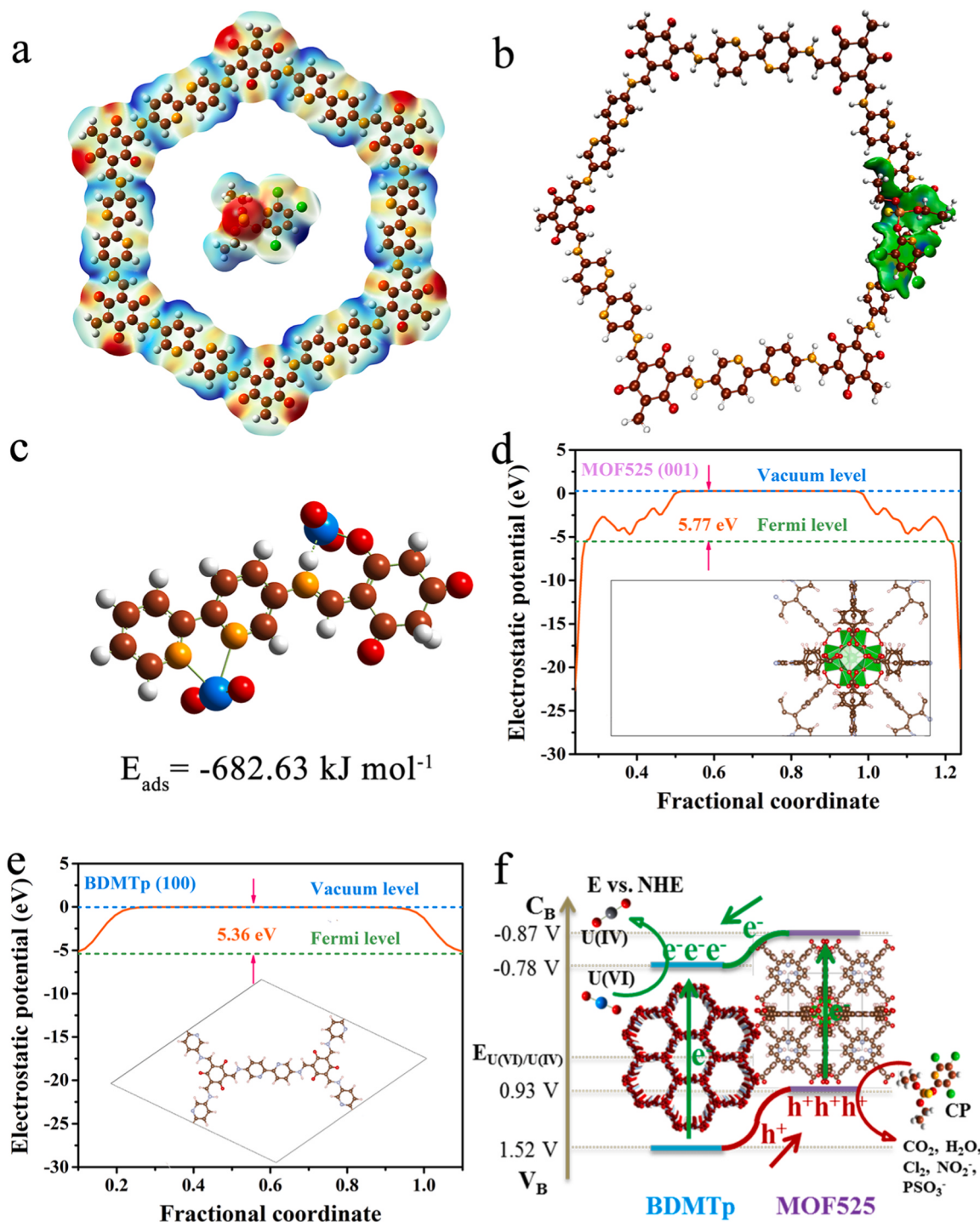


Fig. 5. (a) Van der Waals surface electrostatic potential of BDMTp and CP (Blue area: positive; red area: negative). (b) The IGM plots between BDMTp and CP calculated by DFT. (c) Adsorption energy of partial BDMTp structure and U(VI). Each color ball represents the following elements: brown-red: C, orange: N, red: O, white: H, green: Cl, yellow: S, red-orange: P, and blue: U(VI). The electrostatic potential of (d) MOF525 and (e) BDMTp calculated by DFT. (f) Schematic diagram of photocatalytic removal of U(VI) and CP by MOF525@BDMTp.

94.0% for CP. Therefore, the design of functional integrated composites is an effective means to improve the photocatalytic performance in complex environments.

CRediT authorship contribution statement

Xin Liu: Experiment design, Sample synthesis, Exploration, DFT calculations, Data analysis, Writing – review & editing. **Zhi-Hai Peng,**

and Lan Lei: Investigation, Sample synthesis, Data analysis. **Rui-Xiang Bi, Cheng-Rong Zhang, and Qiu-Xia Luo:** Formal analysis, Validation. **Ru-Ping Liang, and Jian-Ding Qiu:** Conceptualization, Supervision, Funding acquisition, Resources, Writing – review & editing.

Declaration of Competing Interest

The authors declare that they have no conflict of interest.

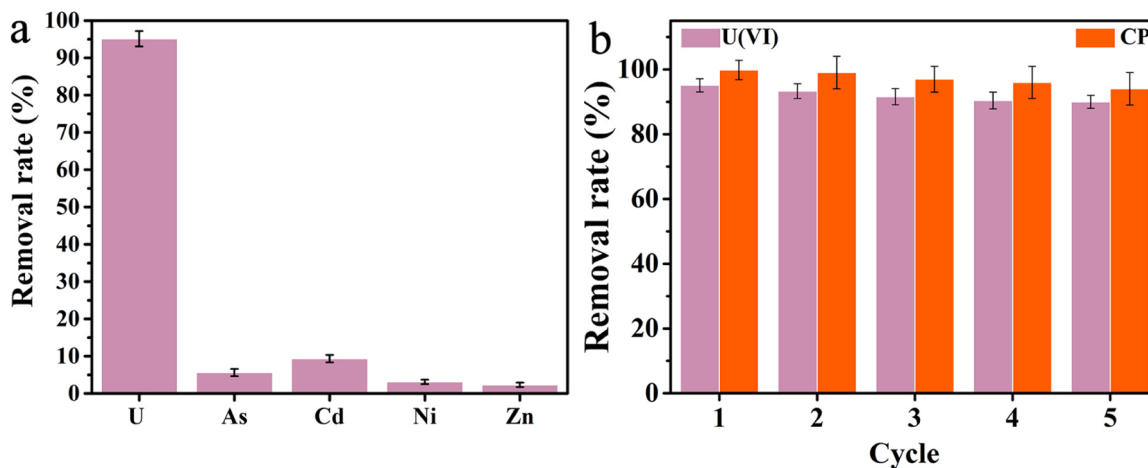


Fig. 6. (a) Ion selectivity and (b) recycling properties of MOF525@BDMTp in wastewater.

Data Availability

No data was used for the research described in the article.

Acknowledgments

We gratefully acknowledge the supports from the National Natural Science Foundation of China (22036003, 21976077 and 22176082) and Natural Science Foundation of Jiangxi Province (20212ACB203009 and 20212ACB203011). Thanks for the reagent supporting from Jilin Chinese Academy of Sciences-Yanshen Technology Co., Ltd. and XPS characterization supporting from Shiyanjia Lab (www.shiyanjia.com).

Supporting Information

Details of the experimental section, conditions optimization, fitting parameters, XPS analysis, and references were in Supporting Information.

Appendix A. Supporting information

Supplementary data associated with this article can be found in the online version at [doi:10.1016/j.apcatb.2023.123460](https://doi.org/10.1016/j.apcatb.2023.123460).

References

- [1] X. Liu, X. Wang, W. Jiang, C.-R. Zhang, L. Zhang, R.-P. Liang, J.-D. Qiu, Covalent organic framework modified carbon nanotubes for removal of uranium (VI) from mining wastewater, *Chem. Eng. J.* 450 (2022), 138062.
- [2] L. Chen, J. Wang, J. Beiyuan, X. Guo, H. Wu, L. Fang, Environmental and health risk assessment of potentially toxic trace elements in soils near uranium (U) mines: a global meta-analysis, *Sci. Total Environ.* 816 (2022), 151556.
- [3] X.-H. Jiang, Q.-J. Xing, X.-B. Luo, F. Li, J.-P. Zou, S.-S. Liu, X. Li, X.-K. Wang, Simultaneous photoreduction of uranium(VI) and photooxidation of arsenic(III) in aqueous solution over g-C₃N₄/TiO₂ heterostructured catalysts under simulated sunlight irradiation, *Appl. Catal. B: Environ.* 228 (2018) 29–38.
- [4] E.M. John, E.M. Varghese, J.M. Shaike, Plasmid-mediated biodegradation of chlorpyrifos and analysis of its metabolic by-products, *Curr. Microbiol.* 77 (2020) 3095–3103.
- [5] Y. Tian, Q. Liu, S. Lin, X. Liang, S. Khan, X. Yang, X. Wang, Magnetic Z-scheme CuFe₂O₄/MIL-101(Fe) toward chlorpyrifos degradation: Photocatalytic mechanism, degradation pathways, and intermediates toxicity evaluation, *J. Environ. Chem. Eng.* 11 (2023), 110054.
- [6] P. Goel, M. Arora, Photocatalytically driven mineralization of chlorpyrifos pesticide by copper nanoparticles, *MRS Adv.* 6 (2021) 774–779.
- [7] F. Silveri, F. Della Pelle, A. Scrocchero, Q.U. Ain, Buhkari, M. Del Carlo, D. Compagnone, Modular graphene mediator film-based electrochemical pocket device for chlorpyrifos determination, *Talanta* 240 (2022), 123212.
- [8] A. Dhakshinamoorthy, Z. Li, H. Garcia, Catalysis and photocatalysis by metal organic frameworks, *Chem. Soc. Rev.* 47 (2018) 8134–8172.
- [9] M.-Y. Zhang, J.-K. Li, R. Wang, S.N. Zhao, S.-Q. Zang, T.C.W. Mak, Construction of core-shell MOF@COF hybrids with controllable morphology adjustment of COF shell as a novel platform for photocatalytic cascade reactions, *Adv. Sci.* 8 (2021) 2101884.
- [10] L. Garzon-Tovar, J. Perez-Carvajal, A. Yazdi, J. Hernandez-Munoz, P. Tarazona, I. Imaz, F. Zamora, D. Maspoch, A MOF@COF composite with enhanced uptake through interfacial pore generation, *Angew. Chem. Int. Ed.* 58 (2019) 9512–9516.
- [11] Y.-P. Wu, W. Zhou, J. Zhao, W.-W. Dong, Y.-Q. Lan, D.-S. Li, C. Sun, X. Bu, Surfactant-assisted phase-selective synthesis of new cobalt MOFs and their efficient electrocatalytic hydrogen evolution reaction, *Angew. Chem. Int. Ed.* 56 (2017) 13001–13005.
- [12] Y. Yao, G. Wu, F. Lu, S. Wang, Y. Hu, J. Zhang, W. Huang, F. Wei, Enhanced photo-Fenton-like process over Z-scheme CoFe₂O₄/g-C₃N₄ heterostructures under natural indoor light, *Environ. Sci. Pollut. Res.* 23 (2016) 21833–21845.
- [13] H. Deng, Z.-J. Li, L. Wang, L.-Y. Yuan, J.-H. Lan, Z.-Y. Chang, Z.-F. Chai, W.-Q. Shi, Nanolayered Ti₃C₂ and SrTiO₃ composites for photocatalytic reduction and removal of uranium(VI), *ACS Appl. Nano Mater.* 2 (2019) 2283–2294.
- [14] Y. Ren, G. Zhou, Z. Lu, Utilization of porous liquids for catalytic conversion, *Chin. J. Struct. Chem.* 42 (2023), 100045.
- [15] S. Chandra, S. Kandambeth, B.P. Biswal, B. Lukose, S.M. Kunjir, M. Chaudhary, R. Babarao, T. Heine, R. Banerjee, Chemically stable multilayered covalent organic nanosheets from covalent organic frameworks via mechanical delamination, *J. Am. Chem. Soc.* 135 (2013) 17853–17861.
- [16] P. Pachfule, A. Acharya, J. Roesser, T. Langenhan, M. Schwarze, R. Schomacker, A. Thomas, J. Schmidt, Diacetylene functionalized covalent organic framework (COF) for photocatalytic hydrogen generation, *J. Am. Chem. Soc.* 140 (2018) 1423–1427.
- [17] L. Akyuz, An imine based COF as a smart carrier for targeted drug delivery: From synthesis to computational studies, *Microporous Mesoporous Mater.* 294 (2020), 109850.
- [18] Y. Lan, X. Han, M. Tong, H. Huang, Q. Yang, D. Liu, X. Zhao, C. Zhong, Materials genomics methods for high-throughput construction of COFs and targeted synthesis, *Nat. Commun.* 9 (2018) 5274.
- [19] R.K. Sharma, P. Yadav, M. Yadav, R. Gupta, P. Rana, A. Srivastava, R. Zboril, R. S. Varma, M. Antonietti, M.B. Gawande, Recent development of covalent organic frameworks (COFs): Synthesis and catalytic (organic-electro-photo) applications, *Mater. Horiz.* 7 (2020) 411–454.
- [20] R. Xue, H. Guo, L. Yue, T. Wang, M. Wang, Q. Li, H. Liu, W. Yang, Preparation and energy storage application of a long-life and high rate performance pseudocapacitive cof material linked with –NH₂ bonds, *New J. Chem.* 42 (2018) 13726–13731.
- [21] Y. Li, M. Karimi, Y.-N. Gong, N. Dai, V. Safarifard, H.-L. Jiang, Integration of metal-organic frameworks and covalent organic frameworks: design, synthesis, and applications, *Matter* 4 (2021) 2230–2265.
- [22] W. Morris, B. Voloskiy, S. Demir, F. Gandara, P.L. McGrier, H. Furukawa, D. Cascio, J.T. Stoddart, O.M. Yaghi, Synthesis, structure, and metalation of two new highly porous zirconium metal-organic frameworks, *Inorg. Chem.* 51 (2012) 6443–6445.
- [23] X. Gong, H. Noh, N.C. Gianneschi, O.K. Farha, Interrogating kinetic versus thermodynamic topologies of metal-organic frameworks via combined transmission electron microscopy and X-ray diffraction analysis, *J. Am. Chem. Soc.* 141 (2019) 6146–6151.
- [24] X. Liu, R.-X. Bi, C.-R. Zhang, Q.-X. Luo, R.-P. Liang, J.-D. Qiu, SnS₂-covalent organic framework Z-scheme van der waals heterojunction for enhanced photocatalytic reduction of uranium (VI) in rare earth tailings wastewater, *Chem. Eng. J.* 460 (2023), 141756.
- [25] W.-R. Cui, F.-F. Li, R.-H. Xu, C.-R. Zhang, X.-R. Chen, R.-H. Yan, R.-P. Liang, J.-D. Qiu, Regenerable covalent organic frameworks for photo-enhanced uranium adsorption from seawater, *Angew. Chem. Int. Ed.* 59 (2020) 17684–17690.
- [26] Y. Xu, X. Zhu, H. Yan, P. Wang, M. Song, C. Ma, Z. Chen, J. Chu, X. Liu, Z. Lu, Hydrochloric acid-mediated synthesis of ZnFe₂O₄ small particle decorated one-

dimensional perylene diimide S-scheme heterojunction with excellent photocatalytic ability, *Chin. J. Catal.* 43 (2022) 1111–1122.

[27] M. Zhang, M. Lu, Z.-L. Lang, J. Liu, M. Liu, J.-N. Chang, L.-Y. Li, L.-J. Shang, M. Wang, S.-L. Li, Y.-Q. Lan, Semiconductor/covalent-organic-framework Z-scheme heterojunctions for artificial photosynthesis, *Angew. Chem. Int. Ed.* 59 (2020) 6500–6506.

[28] Z. Lu, B. Li, B. Wei, G. Zhou, Y. Xu, J. Zhang, H. Chen, S. Hua, C. Wu, X. Liu, Nmp-induced surface self-corrosion-assisted rapid spin-coating method for synthesizing imprinted heterojunction photocatalyst anchored membrane towards high-efficiency selective degradation tetracycline, *Sep. Purif. Technol.* 314 (2023), 123609.

[29] X. Liu, R.-X. Bi, F.-T. Yu, C.-R. Zhang, Q.-X. Luo, R.-P. Liang, J.-D. Qiu, D- π -A array structure of $\text{Bi}_4\text{Ti}_3\text{O}_{12}$ -triazine-aldehyde group benzene skeleton for enhanced photocatalytic uranium (VI) reduction, *J. Hazard. Mater.* 451 (2023), 131189.

[30] F. Guo, B. Hu, C. Yang, J. Zhang, Y. Hou, X. Wang, On-surface polymerization of in-plane highly ordered carbon nitride nanosheets toward photocatalytic mineralization of mercaptan gas, *Adv. Mater.* 33 (2021), e2101466.

[31] M. Lu, M. Zhang, C.-G. Liu, J. Liu, L.-J. Shang, M. Wang, J.-N. Chang, S.-L. Li, Y.-Q. Lan, Stable dioxin-linked metallophthalocyanine covalent organic frameworks (COFs) as photo-coupled electrocatalysts for CO_2 reduction, *Angew. Chem. Int. Ed.* 60 (2021) 4864–4871.

[32] G. Zhou, Y. Xu, Y. Cheng, Z. Yu, B. Wei, X. Liu, Z. Chen, C. Li, Z. Lu, Rapid dissociation of high concentration excitons between $[\text{Bi}_2\text{O}_2]^{2+}$ slabs with multifunctional N-Bi-O sites for selective photoconversion into CO, *Appl. Catal. B: Environ.* 335 (2023), 122892.

[33] H. Lin, Y. Liu, Z. Wang, L. Ling, H. Huang, Q. Li, L. Cheng, Y. Li, J. Zhou, K. Wu, J. Zhang, T. Zhou, Enhanced CO_2 photoreduction through spontaneous charge separation in end-capping assembly of heterostructured covalent-organic frameworks, *Angew. Chem. Int. Ed.* 61 (2022), e202214142.

[34] F. Xing, R. Zeng, C. Cheng, Q. Liu, C. Huang, POM-incorporated ZnIn_2S_4 Z-scheme dual-functional photocatalysts for cooperative benzyl alcohol oxidation and H_2 evolution in aqueous solution, *Appl. Catal. B: Environ.* 306 (2022), 121087.

[35] X. Liu, R.-X. Bi, Z.-H. Peng, L. Lei, C.-R. Zhang, Q.-X. Luo, R.-P. Liang, J.-D. Qiu, Synergistic effect of double schottky potential well and oxygen vacancy for enhanced plasmonic photocatalytic U(VI) reduction, *J. Hazard. Mater.* 455 (2023), 131581.

[36] L. Liu, X.-X. Wang, X. Wang, G.-J. Xu, Y.-F. Zhao, M.-L. Wang, J.-M. Lin, R.-S. Zhao, Y. Wu, Triazine-cored covalent organic framework for ultrasensitive detection of polybrominated diphenyl ethers from real samples: Experimental and dft study, *J. Hazard. Mater.* 403 (2021), 123917.

[37] L. Liu, X.-X. Wang, F. Liu, G.-J. Xu, J.-M. Lin, M.-L. Wang, Y.-N. Wu, R.-S. Zhao, X. Wang, Cationic covalent organic nanosheets for rapid and effective detection of phenoxy carboxylic acid herbicides residue emitted from water and rice samples, *Food Chem.* 383 (2022), 132396.

[38] W.-R. Cui, C.-R. Zhang, W. Jiang, F.-F. Li, R.-P. Liang, J. Liu, J.-D. Qiu, Regenerable and stable sp^2 carbon-conjugated covalent organic frameworks for selective detection and extraction of uranium, *Nat. Commun.* 11 (2020) 436.

[39] Y. Li, X. Guo, X. Li, M. Zhang, Z. Jia, Y. Deng, Y. Tian, S. Li, L. Ma, Redox-active two-dimensional covalent organic frameworks (COFs) for selective reductive separation of valence-variable, redox-sensitive and long-lived radionuclides, *Angew. Chem. Int. Ed.* 132 (2020) 4197–4204.

[40] P.-I. Liang, L.-y Yuan, H. Deng, X.-c Wang, L. Wang, Z.-j Li, S.-z Luo, W.-q Shi, Photocatalytic reduction of uranium(VI) by magnetic ZnFe_2O_4 under visible light, *Appl. Catal. B: Environ.* 267 (2020), 118688.

[41] X. Zhang, Y. Liu, Y. Jiao, Q. Gao, P. Wang, Y. Yang, Enhanced selectively removal uranyl ions from aqueous solution by Fe@ZIF-8 , *Microporous Mesoporous Mater.* 277 (2019) 52–59.

[42] T.S. Anirudhan, F. Shastry, V.C. Sekhar, V.S. Athira, Highly efficient photocatalytic degradation of chlorpyrifos in aqueous solutions by nano hydroxyapatite modified CFGO/ZnO nanorod composite, *J. Photochem. Photobiol. A: Chem.* 418 (2021), 113333.

[43] I. Matanovic, K. Artyushkova, M.B. Strand, M.J. Dzara, S. Pylypenko, P. Atanassov, Core level shifts of hydrogenated pyridinic and pyrrolic nitrogen in the nitrogen-containing graphene-based electrocatalysts: In-plane vs edge defects, *J. Phys. Chem. C* 120 (2016) 29225–29232.

[44] V.N. Zhitomirsky, S.K. Kim, L. Burstein, R.L. Boxman, X-ray photoelectron spectroscopy of nano-multilayered Zr-O/Al-O coatings deposited by cathodic vacuum arc plasma, *Appl. Surf. Sci.* 256 (2010) 6246–6253.

[45] Z. Lu, G. Zhou, B. Li, Y. Xu, P. Wang, H. Yan, M. Song, C. Ma, S. Han, X. Liu, Heterotopic reaction strategy for enhancing selective reduction and synergistic oxidation ability through trapping Cr (VI) into specific reaction site: a stable and self-cleaning ion imprinted CdS/HTNW photocatalytic membrane, *Appl. Catal. B: Environ.* 301 (2022), 120787.

[46] H. Liu, J. Chen, N. Wu, X. Xu, Y. Qi, L. Jiang, X. Wang, Z. Wang, Oxidative degradation of chlorpyrifos using ferrate(VI): Kinetics and reaction mechanism, *Ecotoxicol. Environ. Saf.* 170 (2019) 259–266.

[47] G. Zhou, H. Yan, Y. Ren, M. Song, Y. Hang, X. Liu, C. Li, S. Han, Z. Chen, Z. Lu, Construction of internal electric field in imprinted poly (ionic liquid)- TiO_2 composite nanoreactor for improving hole directional enrichment and selective photodegradation, *Compos. Sci. Technol.* 228 (2022), 109657.

[48] A.R. Nandhini, M. Harshiny, S.N. Gummadi, Chlorpyrifos in environment and food: a critical review of detection methods and degradation pathways, *Environ. Sci. Process Impacts* 23 (2021) 1255–1277.